Energy & Environmental Science

Cite this: *Energy Environ. Sci.*, 2012, **5**, 5980

www.rsc.org/ees

PERSPECTIVE

Nanoscale structure measurements for polymer-fullerene photovoltaics

Dean M. DeLongchamp,* R. Joseph Kline and Andrew Herzing

Received 21st September 2011, Accepted 12th January 2012
DOI: 10.1039/c2ee02725a

This review covers methods to measure key aspects of nanoscale structure in organic photovoltaic devices based on polymer-fullerene bulk heterojunctions. The importance of nanoscale structure to the power conversion efficiency and stability of these devices has been recognized, but robust correlations have yet to emerge despite a significant community-wide research investment. Our perspective is that more uniform selection, execution, and interpretation of nanoscale structure measurements will accelerate this endeavor. We will discuss organic bulk heterojunction structural measurements of contemporary interest and importance including vertical stratification, molecular orientation and order, and nanoscale morphology. Specific recommendations are made regarding the technical implementation of some popular techniques, with an eye toward the elimination of artifacts, ambiguous data, and misinterpretation. When possible, topics are highlighted where there is a community consensus on the results of nanoscale structure measurements and how they may relate to organic photovoltaic device performance.

1. Introduction

Organic Photovoltaic (OPV) devices have emerged in recent years as a promising means to harvest solar energy.[1–4] The principal advantage that OPV devices hold over more traditional photovoltaic technologies is that most or all of the layers of the device can be processed from a liquid solution or dispersion. The fabrication of OPV devices could therefore borrow coating and patterning methods developed for the graphic arts. The most attractive implementations of these methods involve continuous production on a flexible web in so-called "roll-to-roll" production, which may substantially lower the cost of photovoltaic module production. A second merit of OPV technology is the potential mechanical flexibility of the device layers, which may enable innovative new products involving fabrics or plastics that exploit the flexible form factor.

Despite significant gains over the last year with single-junction power conversion efficiencies approaching 10%,[5] the pace of

National Institute of Standards and Technology, 100 Bureau Dr., Gaithersburg, Maryland, 20899, United States

Dean M. DeLongchamp

Dean M. DeLongchamp leads the Organic Electronics and Photovoltaics project in the Polymers Division at the National Institute of Standards and Technology (NIST). He received his Ph. D. from MIT in 2003 for developing self-assembled polymer films with applications in displays, batteries, and fuel cells. His current research is focused on understanding the relationship between device function and the nanoscale structure at organic semiconductor interfaces with advanced measurement methods such as NEXAFS spectroscopy.

R. Joseph Kline

R. Joseph Kline is a staff scientist in the Polymers Division at the National Institute of Standards and Technology (NIST). He received a Ph.D. in Materials Science and Engineering at Stanford University in 2005 for determining the effect of semiconducting polymer molecular weight on charge transport and morphology. His research interests include the development and application of synchrotron-based X-ray diffraction and scanned probe microscopy for morphology characterization of organic semiconductors.

OPV technology development has been slower than expected because its key advantage, solution processability, has led to significant challenges in controlling nanoscale structure formation. Simply put, the structure of a functional layer develops "as the ink dries," and the final result can be significantly influenced by formulation and processing parameters as well as the characteristics of the component materials. Because functional films for organic electronics have specific nanoscale structure requirements, significant and expensive effort has been required for both materials and process design towards the goal of creating a reliable and manufacturable OPV technology. In the ongoing endeavor to increase the overlap of the absorbance of an OPV device with the solar spectrum, and thus harvest a greater fraction of available solar energy, it is commonly discovered that small covalent chemical changes to the active layer materials will comprehensively change their solidification behavior. As a result, many systems that initially appear promising from the perspective of absorbance spectrum or electronic energy levels will, after an exhaustive process optimization effort, never attain their initial promise - an outcome that is often attributed to suboptimal nanoscale structure.[6–8]

The most demanding nanoscale structure requirements in organic electronics technology today are those of the bulk heterojunction (BHJ) photovoltaic active layer. The solution-processed BHJ is a blend of two materials, the first of which is an electron donor and often the strongest light absorber. This material is typically a conjugated polymer, though small molecules are certainly promising as well.[9,10] The second material of the BHJ blend film is an electron acceptor, which is typically a fullerene derivative. The BHJ blend film must be of sufficient thickness (typically > 80 nm) to harvest a significant amount of solar radiation. It must also provide a large interfacial area between the electron donor and electron acceptor phases to facilitate exciton separation. Typical exciton diffusion distances require the electron donor phase to have at least one dimension less than ≈ 20 nm. In addition, charge collection requires that the phases be bicontinuous and well-connected to the correct interfacial layer.[11,12] Throughout this article we will refer to the most well-studied BHJ system, which is the poly-(3-hexyl thiophene): [6,6]-phenyl-C_{61}–butyric-acid-methyl-ester (P3HT:PCBM) blend, unless otherwise noted. More detail on these nanoscale structure requirements has been published elsewhere,[4,6,13] and the importance of nanoscale morphology in OPV has been emphasized in a variety of excellent recent reviews.[2,8,14–19]

Despite the growing recognition of the importance of nanoscale morphology in BHJ operation, it is uncomfortably common to find reports that contradict one another. An example of this can be seen in a recent meta-study of the dependence of P3HT:PCBM device performance on formulation and processing over the past decade.[20] The OPV community has therefore not yet arrived at general process-structure-property relationships that would be of great value in designing new BHJ materials or processes. It is our perspective that more uniform application of nanoscale structure measurement methods will result in more agreement between the results reported by disparate groups, and enable the field to more quickly develop these relationships. In this article, we will focus on three key aspects of nanoscale structure in OPV materials: vertical stratification, molecular orientation and order, and nanoscale morphology. We will discuss the appropriate application and interpretation of measurement techniques for each of these structural aspects. In some cases, we will recommend against certain measurements for which the results are especially ambiguous or not relevant. It is not our intention to challenge published literature on nanoscale structure measurements of the organic BHJ. Rather, we hope to provide a guide that might enhance knowledge and awareness going forward to enable the development of deeper processing-structure-property relationships and better take advantage of the important renewable energy opportunity that OPV represents.

Andrew Herzing

Andrew Herzing received his Ph.D. in Materials Science from Lehigh University in 2007 under the supervision of Prof. Christopher Kiely. He was subsequently awarded a National Research Council postdoctoral fellowship to study the nano- and atomic-scale characterization of materials using transmission electron microscopy and microanalysis techniques at the National Institute of Standards and Technology (NIST) in Gaithersburg, MD. Currently a staff scientist in NIST's Material Measurement Laboratory, he is developing techniques to enable the two- and three-dimensional chemical analysis of nanostructures at ultrahigh spatial resolution, and their application to systems such as organic photovoltaic devices and heterogeneous catalysts.

2. Vertical stratification

We will use the term vertical stratification to refer to any non-uniform distribution of the BHJ components in the direction parallel to the film normal. It has been recognized for quite some time that vertical stratification occurs in BHJ blend films. It was reported in 2005, for example, in relation to charges in device behavior upon annealing.[21] This phenomenon is also referred to as segregation or phase separation, although it does not require a spinodal decomposition process to occur. Typically, a component of the BHJ will become enriched at the top and/or bottom film interfaces relative to its formulation or bulk composition. The predominant concern over vertical stratification is related to charge extraction from the OPV device; electron-transporting material at the anode might block hole extraction, and hole-transporting material at the cathode might block electron extraction. Much work describing interfacial charge extraction in polymer-fullerene BHJs[22] and the potential role of vertical stratification addresses this concern.[23] There are three broad classes of measurements that are most often used to evaluate vertical stratification, as illustrated in Fig. 1: surface analysis methods, whole-film beam reflection depth profiling, and sputter depth profiling.

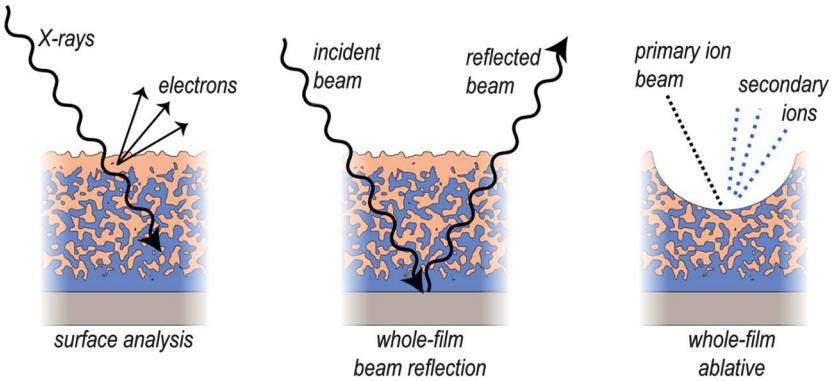

Fig. 1 Three broad classes of vertical stratification measurements for polymer-fullerene BHJ films.

2.1. Surface analysis

Surface analysis techniques include X-ray photoelectron spectroscopy (XPS[24]) and near-edge X-ray absorption fine-structure (NEXAFS[25]) spectroscopy. In these techniques, an X-ray beam of controlled energy is incident on the film surface, and the resulting electron signal is measured to determine the elemental or molecular composition of the interface. The strength of these techniques is that they are generally unambiguous; the sulfur signal in XPS is diagnostic of the presence of thiophene-based polymers, and the carbon K-edge NEXAFS spectra of polymers and fullerenes are easily distinguished,[26,27] permitting quantitative interface composition measurement. The principal ambiguities that may arise are surface contamination and degradation, because these techniques are confined to the first few nanometres of the available surface. Both techniques measure the energy of electrons that have a limited inelastic mean free path (*e.g.* $\approx$ 2 nm), such that the signal is dominated by electrons originating within less than 10 nm of the free surface. Both XPS and NEXAFS have limited near-surface depth profiling capability using grid bias control for NEXAFS or angle-resolved collection for either technique. XPS and NEXAFS spectroscopy have been applied to the top interfaces of a variety of polymer-fullerene BHJ systems, with the universal finding of polymer enrichment at the top (air) interface regardless of the substrate composition, after film casting.[28–37] Segregation beneath a top metal electrode has been investigated by Chen *et al.* using surface analysis after dissolving the aluminum metal with an aqueous solution of copper(II) chloride;[38] it was found that fullerene would segregate to the metal interface if the device was annealed after metallization. This work illustrates a chief limitation of surface analysis methods in the investigation of vertical stratification: probing buried interfaces requires a destructive means to expose the interface to the X-ray beam.

The buried bottom interface of the BHJ is generally more difficult to measure by surface analysis than the top. On model dielectric surfaces, a delamination method using a plastic or elastomeric superstrate has been successful.[29] However, in real OPV device stacks, the bottom interface composition typically cannot be measured due to remarkably persistent contamination by the poly(3,4-ethylenedioxythiophene): poly(styrenesulfonate) (PEDOT:PSS) anode material upon delamination.[28,31,36] On model dielectric surfaces, the fullerene material segregates to substrates with higher surface energy, whereas the polymer segregates to the substrate with lower surface energy, suggesting that the vertical stratification is due to the surface energy differences between P3HT ($\approx$ 27 mN m^{-1}), and PCBM ($\approx$ 38 mN m^{-1}).[29,36] This result further suggests that the moderate surface energy PEDOT:PSS ($\approx$ 45 mN m^{-1}) might attract fullerene. Most vertical stratification measurements by surface analysis agree that it occurs as relatively thin "skin" layers enriched in either component, not as a gradual gradient of composition throughout the film thickness.

2.2. Beam reflection

Another class of methods to examine vertical stratification is based on reflected beams. The most common of these methods that have been applied to BHJs are neutron reflectivity (NR[39]) and variable angle spectroscopic ellipsometry (VASE[40]). Because reflected beams penetrate the whole film stack before reflection, this class of techniques can provide information about buried interface composition without the need for etching or delamination. These techniques are model-dependent, however, and vertical stratification is determined by forward simulating the intensity (and polarization characteristics in VASE) of the reflected beam as a function of incident angle and/or wavelength using a detailed physical model, and then comparing the simulated values to experimental data to refine the model in an iterative fitting procedure. Although these techniques are more ambiguous than surface analysis due to the challenge of proving model uniqueness, they can provide a whole-film vertical stratification measurement, often referred to as a depth profile.

NR commonly requires isotopic labeling (deuteration) to discriminate between two hydrocarbon materials with similar proton densities. In polymer-fullerene BHJ systems, however, NR can exploit the intrinsic differences in proton density between a polymer (many protons) and fullerene (few protons), which results in a large neutron scattering length density contrast without further labeling. For P3HT/PCBM BHJ films, the depth profiles provided by this method have differed depending on the team. Kiel and co-workers find an enrichment of PCBM at a high surface energy model dielectric interface, consistent with surface analysis results,[41,42] but the dominant contribution at the air interface surprisingly appears to be PCBM as well. Parnell and co-workers, on the other hand, see PCBM enrichment at the high surface energy dielectric and polymer enrichment at the top

interface, in a result that is wholly consistent with the surface analysis literature, as shown in Fig. 2a.[43] Challenges in model development for NR can arise from lateral heterogeneity, either in the film bulk or appearing at the top interface as surface roughness. Roughness can lead to misidentification of the top surface composition because it can lower its apparent scattering length density, essentially because solid matter is mixed with air at a rough interface. It must be noted that the published NR depth profiles, like surface analysis methods, typically show a uniform bulk with thinner segregated skin layers.

We note that X-ray reflectivity (XRR) shares the same basic principles as NR, albeit with an incident X-ray beam. The scattering length density of organic matter in XRR performed with a typical fixed energy source (such as Cu-Kα radiation) is roughly proportional to mass density. Thus for films with an appreciable change in density between the amorphous and crystalline phases, a potential ambiguity exists in discriminating composition from crystallinity. Both P3HT and PCBM, for example, are capable of crystallizing. If either crystalline phase is significantly more dense than its corresponding amorphous phase, then vertical variations in crystallinity could be misinterpreted as vertical composition stratification. This ambiguity is similar to that of bright-field transmission electron microscopy, which we will discuss further in section 4.1. A potential solution to contrast ambiguity in XRR is the use of resonant soft X-ray reflectivity (RSoXR), which has recently seen application in the study of organic semiconductor film multilayers.[34,44,45] In RSoXR, organic components can be discriminated by the selection of an incident wavelength near the carbon K-edge where the scattering length density contrast is maximized. It is a powerful emerging technique that may provide information similar to that from NR without the need for isotopic labeling.

VASE is perhaps the most accessible method with which to measure vertical stratification in organic BHJs, because it is a benchtop instrument with a relatively low capital cost. In general, however, the technique has seen relatively little use in organic BHJ measurement, most likely due to challenges in properly modeling the indices of refraction of the BHJ components. Recent work on VASE of the BHJ has shown that both vertical stratification and optical anisotropy are important to the VASE model,[36,46] but optical anisotropy is more important than stratification to the quality of fit.[36] Optical anisotropy, which refers here to different film refractive indices in the in-plane and out-of-plane directions, typically results because most conjugated polymer backbones align parallel to a substrate when spin-coated. The anisotropy of the refractive index of a BHJ can be extremely large, as demonstrated in Fig. 3. This anisotropy is critical to the VASE model, because if an isotropic refractive index is assumed, the best model fit to a constrained linear profile is usually found to be a composition gradient, which has been reported before.[47,48] Additionally, this anisotropy is critical to the correct description of the absorption of light in OPV devices (*e.g.*, by conventional UV-Vis absorption spectroscopy). The absorbance of normally incident, unpolarized light of a film with perfect in-plane orientation of the polymer backbone will be 1.5 times that of the equivalent isotropic film. Using an anisotropic P3HT refractive index and permitting three layers produces a model fit that is consistent with these other techniques.[36] Fig. 2b shows the model profile with a best-fit model structure. We

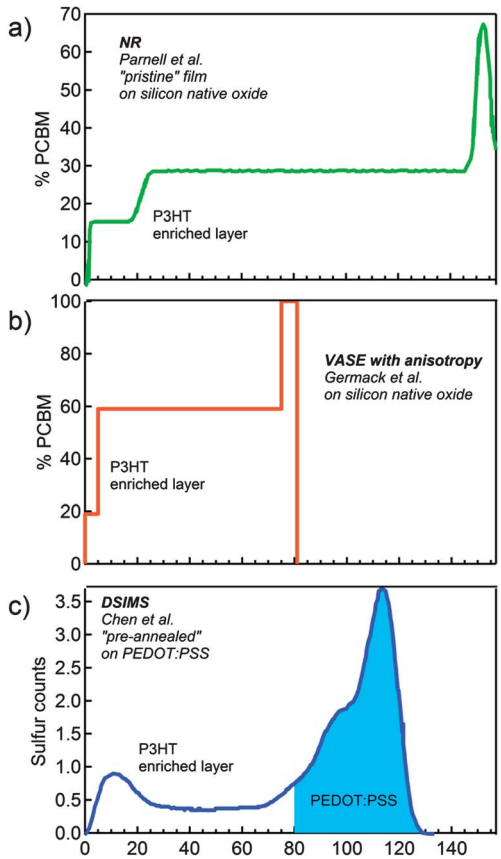

Fig. 2 A comparison of published vertical stratification measurements of the P3HT:PCBM BHJ system provided by whole-film depth profiling techniques including a) NR,[43] b) VASE,[36] and c) DSIMS.[38] The distance coordinates in b are approximate. For all techniques, a thin P3HT enrichment layer is observed at the surface, with a bulk having uniform composition.

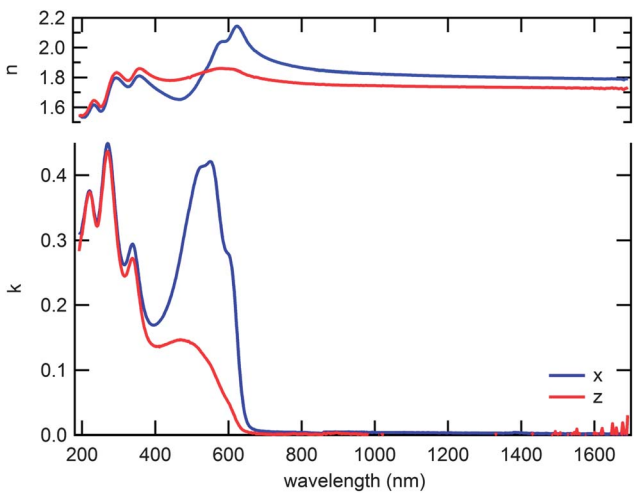

Fig. 3 The best-fit refractive index for a P3HT:PCBM BHJ film on silicon oxide, showing a high degree of anisotropy. n is the real part and k is the imaginary part of the refractive index. Traces labeled x are the refractive index parallel to the substrate, and traces labeled z are perpendicular to the substrate.

strongly encourage the further development of VASE as an accessible and low-cost technique that can simultaneously provide information on film thickness, vertical stratification, and absorbance properties. Indeed, VASE may make an excellent in-line monitoring tool for OPV module production.[48] However, the power and accessibility of VASE is balanced by the requirement for accurate and detailed optical models for every material that will be measured.

2.3. Sputter depth profiling

In sputter depth-profiling, analysis techniques such as XPS, auger electron spectroscopy, or secondary ion mass spectrometry are used in concert with a sputtering action that selectively removes layers of the sample starting from the top interface.[49] Therefore these techniques are not model dependent. Critical to the implementation of these techniques, however, is the optimization of the sputtering. Several issues must be addressed including selective sputtering of one material over another, profile broadening, and sputtering-induced chemical changes. The relationship of sputter time to sputter depth may not be straightforward, and the resolution of the technique is highest for the first sputtering events, and it degrades as the depth profile proceeds downwards due to mixing.

The most common sputter depth profiling technique to be applied to the polymer-fullerene BHJ is dynamic secondary ion mass spectrometry (DSIMS[50]). DSIMS is typically practiced by sputtering the BHJ surface with a focused primary ion beam such as O^+. The ejected secondary ions are then collected and analyzed by mass spectrometry. The primary means to distinguish the polymer and fullerene is the sulfur signal,[51–53] although deuteration of the PCBM can add an additional means for contrast.[38] In general, the vertical stratification reported by DSIMS is consistent with that from surface analysis and model-based depth profiling techniques. Polymer skin layers are typically observed at the air surface, with a uniform bulk composition and some compositional perturbation at the substrate interface, as shown in Fig. 2c. The lower sulfur counts at the surface are due to sample roughness.

2.4. Device implications

The vertical stratification revealed by surface analysis methods reveals that a polymer-fullerene BHJ forms "upside down" with respect to the geometry of a conventional OPV device because the hole-transporting polymer is enriched at the cathode and it is unlikely to be enriched at the anode. The enrichment of polymer at the cathode has been blamed for poor charge extraction,[21,35,54] and there have been attempts to "correct" the anode interface as well.[55] One way to correct the device is the use of an inverted architecture,[56] where the BHJ film is cast on a cathode substrate and an anode is applied to the top, such that the device structure is better matched to the intrinsic segregation of the components.[28,57]

Recent results, however, call into question whether vertical stratification is responsible for a loss in efficiency in conventional OPV devices. Perhaps the most compelling is that inverted devices have thus far not been shown to provide generally enhanced power conversion efficiency over conventional device architectures. Furthermore, a novel experiment in which the BHJ film was cast and then physically inverted *via* a soft lamination method revealed that interfacial segregation had no significant effect on OPV device properties.[58] Finally, it has been confirmed by XPS[59] and NEXAFS spectroscopy[38] that a polymer-fullerene BHJ in the conventional device architecture "re-segregates" when heated to form a PCBM-enriched layer next to its metal cathode. Therefore the top interface of the BHJ should not block electron transport in conventional devices that are heated after electrode application.

Although there is no firm evidence that polymer segregation affects OPV device performance, it has been proven that vertical stratification does affect the stability of a polymer-fullerene BHJ. On high-energy substrates that attract PCBM, micron-scale crystallization is far more prevalent following heating than on low-energy substrates that attract the polymer.[60] The surface energy of the BHJ substrate (typically a hole transport layer in conventional device architectures) will influence to what extent PCBM will crystallize. This effect was exploited to control nanoscale lateral segregation of a polymer-fullerene BHJ by nano-patterning high surface energy patches that nucleated fullerene crystals.[61]

The vertical stratification revealed by surface analysis methods has important implications for the use of scanning probe measurement methods on BHJ films. Topographical atomic force microscopy (AFM) images should not be interpreted as necessarily having a relationship to the bulk BHJ structure for the simple reason that the surface composition does not resemble the bulk. This effect should have some bearing on the interpretation of electrical scanning probe methods as well, since the probed surface may have only a tenuous relationship to the bulk charge transport pathways.[62,63] We note that some recently-developed scanning probe methods may be able to discriminate between surface and subsurface regions,[64] and some may be capable of studying devices near operating conditions.[63,65,66]

2.5. Bilayers

The nano-scale interface between polymer and fullerene is probably the most critical structural feature of a BHJ, but the structure details of this interface are beyond the reach of most measurement methods with the possible exception of nuclear magnetic resonance. Many groups have begun to study bilayers as models for these internal interfaces. The thermal stability of bilayers can provide insight into the fundamental phase behavior of the two materials. Although some work on bilayers used an approach based on solvent orthogonality to make bilayers by sequential solution processing,[67] it was shown that this method produces bilayers that are already quite well-mixed.[68] Most bilayer experiments are now done using physical transfer, either with elastomeric stamps or *via* floating techniques.

With NR[68] VASE,[69] and DSIMS,[34,52,70] it has been shown using bilayer experiments that there is significant diffusion of PCBM into P3HT, even at modest temperatures. These results suggest that the P3HT:PCBM BHJ is not composed of two pure phases; at least one of the phases is a mixture of the two components. This result is supported by work on lateral PCBM diffusion using scanning transmission X-ray microscopy (using the same spectroscopic principles as NEXAFS), where

a significant PCBM presence was found in P3HT.[71] The work on bilayers published thus far reports significant variation in the amount of PCBM uptake at apparent steady state conditions (anywhere from ≈ 10% to ≈ 40% PCBM within the P3HT film), suggesting that variations in the state of the P3HT film such as crystallinity can affect its ability to dissolve PCBM. Surprisingly, it has been shown that diffusion of PCBM into P3HT from a bilayer can result in bulk compositions and device behavior similar to that of a BHJ where both materials are cast from the same solution.[68,72]

3. Order and orientation

3.1. Molecular order and orientation

The term "order" has multiple potential meanings when applied to semiconducting polymers. More often, order refers to the occurrence of spatially repeating atomic locations on a length scale significantly greater than a single molecule, in what would typically be called a crystalline, paracrystalline, or liquid crystalline state. However, the term can also be used to describe the extent of backbone conformational regularity (*e.g.*, ring coplanarity), which is sometimes referred to as "molecular order." This form of order is most often measured optically, with the well-developed aggregate resonances in P3HT proving especially useful for this purpose.[73,74] Molecular order can also be measured by nuclear magnetic resonance (NMR).[75] It is important to note that these two types of order do not necessarily correlate. A polymer that exhibits a high degree of spatially periodic order must, by definition, also be molecularly ordered, but the converse is not necessarily true.

The optical and electrical properties of molecularly ordered semiconducting polymers are typically anisotropic. Thus the orientation of the polymer domains is critical for determining both the absorption in a PV device and the charge transport relevant to charge extraction. The primary optical transition dipole (π–π^*) is oriented along the long axis of the backbone. Consequently, the orientation of the polymer backbone will determine the absorption length of the polymer film. This orientation is reflected in the anisotropy of the refractive index shown in Fig. 3. Charge transport in semiconducting polymers requires a combination of movement of the charge along the conjugated backbone and intermolecular transfer between neighboring molecules. Accordingly, the orientation of the backbone and of the directions of highest intermolecular transfer (usually the π-stacking direction) will determine the anisotropic charge carrier mobility in the film.[76] The exact details of charge transport in semiconducting polymers depend on the specific polymer and are comprehensively described elsewhere.[77,78]

A variety of measurements have been used to measure molecular order and orientation of semiconducting polymer films.[26] Each technique measures a different aspect of the order and orientation, so the answers are not necessarily the same. As described in the previous section, spectroscopy methods can measure the orientation of various moieties of the molecule. NEXAFS can measure the orientation of antibonding orbitals and can determine the average orientation of the side chains through the C–C σ^* orientation or the average tilt of the conjugated backbone through the C–C π^* orientation.[26,27] Recently developed low bandgap molecules contain additional bonds containing N, O, or F that can also be measured with NEXAFS. It should be noted that electron-yield measurements with NEXAFS are surface sensitive, so the measured orientation are within a few nm of the surface. Polarized IR measurements can be used to determine the average orientations of many of the same chemical groups and provides a measurement of the film bulk.[79] VASE measurements have been used to determine the orientation of the π–π^* transition and thus the polymer backbone.[79,80] All three of these techniques are linear spectroscopies and are not sensitive to the orientation distribution. The measured orientations are average orientations that can typically be described by an infinite number of possible orientation distributions, except in cases of strong orientation where the number and character of potential orientation distributions is constrained. Other measurements can be combined with the linear spectroscopy to limit the parameter space and determine a better estimate of the orientation distribution.[26] It should also be noted that these techniques measure all molecules (both amorphous and crystalline) within their sampling space. NEXAFS has no sensitivity to crystallinity while VASE has some sensitivity to crystallinity due to the fact that the imaginary part of the dielectric constant is different for aggregated and amorphous regions. Characterization of the amorphous regions of the film has become especially important for recently developed low bandgap polymers with substantially lower crystallinity than P3HT.

3.2. Spatially periodic order

X-ray diffraction (XRD) is used to measure spatially periodic order. Short-range and long-range order cause X-rays to diffract as a result of their periodicity, repeat distance, and orientation. Diffraction occurs when periodic planes in an ordered material match the Bragg conditions.[81] The scattering angle is related to the spacing of the periodic planes and the orientation of the scattering vector corresponds to the normal of the periodic planes. The short-range and long-range order are described by the correlation function through the decay of the periodicity. Highly ordered regions such as crystals result in a series of higher order scattering peaks for each planar spacing. Scattering from amorphous regions that have a well-defined 1st nearest neighbor spacing (such as glass or PCBM) result in diffuse rings, while amorphous materials with a complex shape (such as low bandgap polymers with complicated monomers), and therefore no well-defined spacing, result in only diffuse background scattering without a ring. Thus the diffraction measurement is dominated by the ordered regions of the film. We will return to this point later in our discussion of absolute crystallinity. XRD does not directly measure molecular orientation; it instead measures the orientation and spacing of periodic planes. The angles between the various planes are used to construct a unit cell and a repeat unit, allowing the orientation of the molecule in the unit cell to be estimated. In most measurements involving semiconducting polymers, the systems are sufficiently disordered that only a few scattering peaks are observed and it is impossible to determine the location of each atom in the unit cell. The primary diffraction peaks observed come from the π–π spacing (≈ 0.4 nm) and the lamellar spacing in the direction of the side chains (≈ 2.0 nm).

For simplicity in systems with few scattering peaks, an orthorhombic unit cell is often assumed, allowing estimates of the crystal orientation distribution.

XRD measurements for OPV films are usually done using either grazing-incidence X-ray diffraction (GIXD) or thin-film XRD geometries. GIXD involves an X-ray beam that impinges upon the sample at an angle of about a tenth of a degree and allows the measurement of scattering planes whose normal is in the plane of the substrate. GIXD is particularly valuable for thin films because the grazing angle localizes the X-ray intensity in the thin film and enhances the normally weak scattering signal. Thin-film XRD primarily measures planes whose normal is close to perpendicular to the plane of the substrate (out-of-plane). Thin-film XRD can measure the orientation distribution by tilting the sample at a fixed scattering angle (rocking curve). Rocking curves and GIXD data can be combined to obtain a full pole figure (orientation distribution plot) of the ordered regions in the film.[82] The pole figure is the scattered intensity distribution over a fixed solid angle, so the pole figure for a 3D isotropically oriented thin film would be flat. It should be noted that the pole figure is not the fraction of crystals at a given tilt angle for a thin film that is isotropically oriented in-plane. As shown in Fig. 4, due to the geometry of a film, the solid angle of crystals at a given azimuthal tilt increases as the azimuthal tilt increases through the product of the sine of the azimuthal tilt and the pole figure intensity at that tilt.[83,84] It is thus clear that the pole figure measurement on films undercounts the number of crystals with their planes oriented near in-plane. This is particularly important for solar cells, since the primary concern is the full orientation distribution of the crystals. In many cases inaccurate pictures are drawn suggesting that the films contain considerably more oriented crystals than is the actual case. Finally, when determining relative crystallinity or estimating the fraction of the film that has a given azimuthal orientation, the pole figure must be integrated around all possible in-plane orientations to count all the crystals in the film.[84,85] Relative crystallinity numbers extracted from pole figures are commonly reported for BHJ samples. Absolute crystallinity, on the other hand, is nontrivial and rarely reported correctly. The difficulty lies in the fact discussed earlier that the amorphous scattering in semiconducting polymers is quite weak and diffuse compared to the crystalline scattering. In conventional polymers, the absolute crystallinity is often determined by using 100% and 0% crystalline standards and using a linear combination of the two to determine the crystalline fraction of the unknown sample. The lack of measureable scattering from amorphous samples and the inability of producing a 100% crystalline sample preclude the use of the linear combination method in most conjugated polymer thin films.

The effect of azimuthal tilt combined with a partially oriented sample can result in a common misinterpretation of GIXD data. In particular, the appearance of an arc that appears predominantly oriented out-of-plane is often attributed to an oriented crystal population, but it can also result artificially from a 2D powder with the third axis constrained to the sample plane. In the case of semiconducting polymers, it is quite common to have the polymer long axis of crystals (**c**) oriented in the sample plane (see earlier discussion on VASE). When this occurs, the possible orientation distributions of the other axes (**a** and **b**) are forced to be equal and more vertical because they are complementary. The best example of this geometry would be an array of logs that are free to rotate along both their long and short axes but are

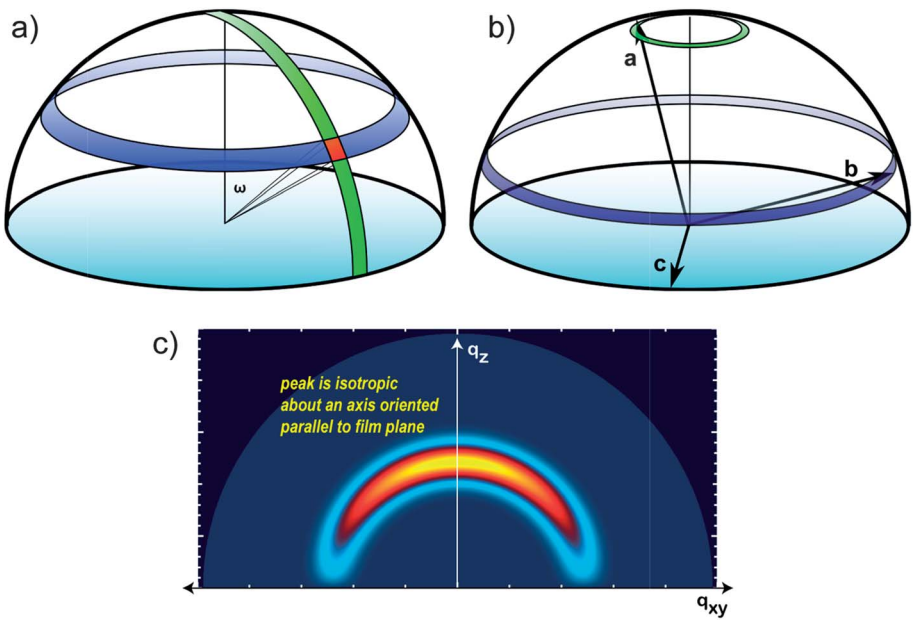

Fig. 4 a) Diagram showing the population of crystals as a function of the azimuthal tilt angle ω. The blue ring shows the total solid angle of crystals at the chosen tilt angle, the green band shows the range of the crystals measured in the rocking curve and the red region denotes the solid angle of crystals measured at the current tilt. b) Diagram showing the coupling of **a** and **b** axis when the **c** axis is constrained to the sample plane. The number of crystals in the blue and green rings must be equal, resulting in a higher density for vertically oriented planes. C) Simulated GIXD of a diffraction peak that has no preferred orientation. The appearance of orientation in the arc is due to the combination of the thin film geometry and the constraint of one axis to the sample plane.

confined to have their long axis in-plane. The confinement of the long axis to the sample plane reduces the likelihood that either of the short axes will be oriented in-plane. The end result is that orientation distributions for **a** and **b** in a 2D powder with the third axis constrained to the sample plane will be isotropic as function of total population at a given azimuthal tilt angle and not at a fixed solid angle (what is measured by a pole figure). This means that pole figures will artificially show a preferential vertical orientation. Fig. 4c shows a simulated diffraction pattern for a 2D powder with the third axis confined to the sample plane. Conversion of the pole figure into a plot of the crystal population *versus* azimuthal tilt greatly aids the interpretation of the orientation distribution. Knowledge of the orientation of the other two axes is required to fully determine the crystal orientation of this sample. Unfortunately for the case of P3HT, the scattering from the **c** axis is weak and usually not observed. Orientation information derived from complementary measurements such as VASE and NEXAFS can be used to aid the interpretation of the orientation distribution. This example underscores the general need for rigorous mathematical analysis of GIXD data; appraisal of the pattern "by eye" can be extremely misleading.

GIXD is commonly applied to BHJ films to determine the crystal structure, crystal orientation, and relative crystallinity of both the polymer and the PCBM. GIXD allows the *in situ* measurement of these parameters as a function of annealing or film drying.[70,86,87] Numerous studies have investigated the effects of thermal annealing on the crystallization of PCBM from its initial amorphous state. The PCBM crystallization was found to be dependent on the surface chemistry of the substrate,[60] revealing potential problems when films for X-ray analysis are deposited on glass or silicon wafers to simulate device films that are deposited on PEDOT:PSS. Fig. 5 shows an example from Gomez *et al.* of how GIXD of P3HT:PCBM films can be used to determine changes in crystallinity with annealing.[84] In the not annealed sample, the PCBM scattering is a diffuse ring caused by amorphous PCBM. The P3HT scattering consists of an edge-on series of the (H00) peaks from the lamellar stack along the q_z direction and an arc near the horizon at $q_{xy} = 1.65$ Å^{-1} due to the (010) scattering from the π-stacking direction. The arcs are indicative of a broad orientation distribution of the P3HT crystals. Annealing causes the PCBM to crystallize as shown by the appearance of a sharp ring on top of the diffuse PCBM ring. The sharpness indicates relatively large crystals and the ring indicates that the crystals have near random orientation. It should be noted that in some cases the PCBM crystals formed during annealing are preferentially oriented.[60,86] The 2D image shows a qualitatively similar orientation distribution of the P3HT to the not annealed film and an increased intensity. To quantify this, a full pole figure must be done (Fig. 5d). The pole figure shows that the crystallinity has increased three-fold and that the orientation distribution has broadened with annealing.

4. Nanoscale morphology

The organic BHJ film requires a close match between the length scale of the donor/acceptor phase separation produced during fabrication and the exciton diffusion lengths typical of semiconducting polymers ($\approx$10 nm to 20 nm).[4,6,13] Characterization of the morphology of high-efficiency device films is a challenging measurement science problem that few techniques can address. AFM could provide the required spatial resolution, but it is only sensitive to morphological details present at the film surface and the composition at the film surface almost never resembles that of the bulk, as we discuss in section 2.1. While AFM methods have their place, we strongly caution against sole reliance on topographical AFM for characterizing nanoscale morphology in BHJ films. Instead, a technique that is capable of imaging the morphological characteristics of the film bulk at a similar high spatial resolution is required. In recent years, the transmission

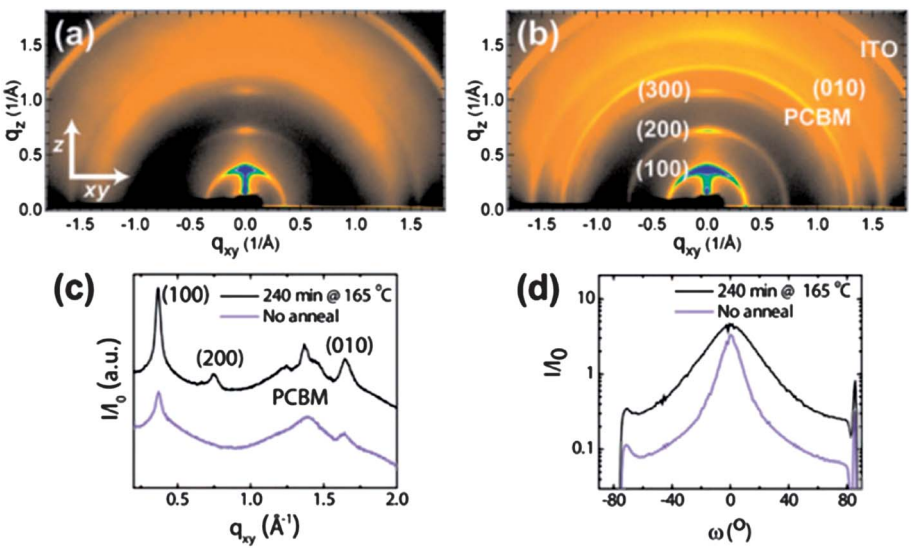

Fig. 5 Two-dimensional grazing-incidence X-ray diffraction images of P3HT/PCBM films (a) not annealed and (b) annealed at 165 °C for 240 min. The films were cast on PEDOT: PSS/ITO to resemble the structure of the active layer in solar cells. (c) In-plane radial traces of GIXD data from (a) and (b) taken at qz = 0.1 Å–1. The data from the annealed film are shifted along the *y*-axis for comparison. (d) Full pole figures of the P3HT scattering for the same P3HT/PCBM films as a function of the polar angle, ω.[84]

electron microscope (TEM) has emerged as the most powerful technique to meet this need.

TEM has long played a central role in the nanoscale characterization of both inorganic and organic matter. The ability to characterize the structural, morphological, and, when coupled with electron energy-loss spectrometry, *chemical* features of an as-deposited organic thin-film specimen at nanometre length scales makes it an indispensible tool for developing structure-property correlations. Furthermore, while TEM images are inherently two-dimensional projections through the thickness of the specimen, it is possible to acquire structural and chemical information in 3-D *via* electron tomographic techniques. In this case, many projection images are acquired from the same area of interest over a wide range of specimen orientations. This series of images is then used to reconstruct a 3-D representation of the full analytical volume of the film. While this technique has been used for many decades in the biological community, recently its utility for organic and solid state materials science has been heavily explored as well.[88] Electron tomography techniques are ideally suited for the characterization of BHJ systems, since they are generally thought to consist of a 3-D network of two materials which are organized at the nanoscale.

4.1. Bright-field TEM

Generally speaking, any image or spectroscopic signal that can be collected in the TEM can be used as the basis for electron tomography, as long as it obeys the projection requirement that the signal varies monotonically with tilt and thickness. The most common signal used for carrying out 3-D tomographic analysis is the bright-field (BF) image signal. In an amorphous material, the contrast generated in this mode is primarily due to incoherent, elastic scattering of the incident electrons by the Coulomb field of the nuclei within the specimen. The cross-section for such scattering is heavily dependent upon the mass of the scattering atoms, and thus regions of the specimen containing atoms with a higher atomic number will appear to be darker than those containing only low atomic number elements. The BF-TEM approach has the advantages of producing a data set with a high signal to noise ratio as well as being relatively simple to acquire. Indeed, many software packages are now available which fully automate the data acquisition process.

In several recent papers, the Loos group has successfully applied BF-TEM tomography to OPV systems such as P3HT:PCBM,[89] MDMO-PPV:PCBM,[14] and PF10TBT:PCBM.[90] An example of this work is shown below in Fig. 6, which summarizes the results of an electron tomographic reconstruction of a P3HT:PCBM blend film. The film was spin cast from an *ortho*-dichlorobenzene solution (1 : 1 by mass) with a slow drying procedure, and subsequently annealed at 130 °C for 20 min. The images are slices extracted from near the top, middle, and bottom of the film (Fig. 6a, b, and c, respectively). Elongated fibrils ascribed to P3HT crystals are present to varying degree in all slices. However, careful measurement of the area fraction of fibrils at each slice suggests that vertical segregation of P3HT crystals occurred during processing.

Despite these impressive results, the BF-TEM signal is not universally suited as a basis for electron tomography of OPV films. This arises from a number of factors, the first of which concerns difficulty in interpreting the contrast exhibited by the images. As discussed previously, the enhanced scattering of the electron beam by areas of the specimen with relatively higher mass produces differential contrast in the image between such regions. However, since the mean-free-path of the electrons at a given voltage is fixed, an increase in scattering is also produced by increases in thickness, and the contributions of these two contrast mechanisms can be very difficult to deconvolute. This is particularly troublesome in films which exhibit enhanced roughness, such as those often encountered in spin-cast BHJ films, because any deviation from a perfectly flat film will produce contrast changes due to thickness fluctuations and this will complicate the image interpretation.

In crystalline specimens, contrast interpretation can become more complex because BF-TEM images will also exhibit strong contrast due to Bragg diffraction. This causes intensity to be scattered out of the image from areas of the specimen that are at or near the Bragg angle, and such regions will then appear dark in the resulting image. Obviously, this effect is orientation dependent and therefore does not obey the projection requirement for tomography since sudden changes in contrast will occur over the course of the tilt-series acquisition. This pitfall can often be avoided for BHJ analysis since the constituent materials tend to be poorly ordered, and, if the specimen is being analyzed under non-cryogenic conditions, the structure of even a well-ordered organic crystal will significantly degrade due to radiation damage over the course of a tilt-series acquisition.

Finally, an organic BHJ film consisting of an intimate mixture of two materials with comparable compositions and densities

Fig. 6 Results of a BF-TEM based electron tomography analysis of a P3HT:PCBM BHJ film after a 3 h solvent-assisted annealing treatment. Images were extracted from the resulting electron tomogram at varying vertical positions through the thickness of the film: near the top of the film (a), near the middle of the film (b), and near the bottom of the film (c). The field of view is approximately 1700 nm.[89]

such as P3HT and PCBM is particularly challenging in terms of BF-TEM image interpretation. Scattering theory predicts that the increased density of PCBM relative to P3HT would produce differential contrast in a BF-TEM image of the two materials side-by-side. However, in a BHJ the characteristic length scale for phase separation is typically a small fraction of the total film thickness ($\approx$15 nm compared to 100 nm), such that the effective density projected through any given point in the film lies between that of the constituent materials. Furthermore, since the phase separation in a high-efficiency device is nearly isotropic, the effective density will be nearly the same at all points in the film and very little mass-thickness contrast will be observed in the BF-TEM image.

Scattering from low-Z materials can be increased by lowering the acceleration voltage of the incident beam, however, this only enhances the overall scattering from the film and will not produce greater differential contrast as this depends only on the number and identity of the atoms present. Furthermore, choosing a voltage of 80 kV *versus* 300 kV exacerbates the attenuation of the electron beam by the specimen. While this may not be a problem for imaging at a plan-view orientation, the effective thickness at the high-tilt values required of electron tomography can be significant enough to render the specimen opaque. To illustrate this issue, consider a thin film of carbonaceous material with a uniform thickness of 100 nm. At a specimen tilt of 70° with respect to the electron beam, the effective thickness is 292 nm. Since the mean free path of 80 kV and 300 kV electrons in such a material is $\approx$ 115 nm and $\approx$ 210 nm, respectively, on average the 80 kV electrons will have undergone 3 scattering events before exiting the specimen while the 300 kV electrons will have undergone only 1. This will result in a severe loss of signal in the 80 kV case at high tilt, and will also produce blurring due to the effects of chromatic aberration.

Another method commonly employed for increasing contrast in BF-TEM images involves the application of a certain amount of defocus to the objective lens.[91] This method alters the contrast transfer function of the lens, and enhances the phase contrast produced at specific spatial frequencies. However, this comes at the expense of spatial resolution since any structural features which are smaller than the selectively enhanced features will be blurred or lost in the image. It can also lead to difficulty in contrast interpretation, as the added phase contrast can produce artifacts in the image and because the image contrast is now a convolution of mass, thickness, and phase-contrast. This is illustrated in the series of images presented in Fig. 7 of a P3HT:PCBM blend film. At Gaussian focus (0 μm), little contrast is present in the image, save that of the large (*i.e.* 150 nm to 200 nm) isolated regions of light and dark intensity. These features are due to increased scattering out of the image in the dark regions, and could be related to, among a number of causes, changes in thickness, local enrichment of the relatively heavier PCBM phase, or differences in crystallinity. Definitively ascribing them to one or another of these causes is non-trivial. By applying various levels of defocus (Fig. 7(b) and (c)), features at the expected 10 nm to 20 nm size regime are enhanced, however, the phase contrast responsible for this enhancement may or may not be related to the underlying morphology.

4.2. Energy-filtered TEM

An alternative image signal based on inelastic, chemically-sensitive scattering is being explored by our group as a viable means of more robustly and perhaps quantitatively characterizing the 3-D structure of OPV films. This is done using energy-filtered TEM (EF-TEM) imaging, which involves energetically dispersing the transmitted beam of electrons and forming an image using only those electrons which have lost a specific amount of energy. Since the contrast in this mode is related directly to the chemical or electronic makeup of the specimen at any given point in the image, no contrast enhancement is necessary. Therefore, the objective lens can be set to Gaussian focus values, preserving the spatial information at all the relevant length scales, and the analysis can be carried out on thicker specimens since lower accelerating voltages are not necessary to produce contrast.

This type of spectroscopic imaging has been used in the past to distinguish between the constituents in a multi-phase, organic system. Specifically, Libera and co-workers have used EELS mapping of two phase nanocolloids[92] and multiphase polymer blend materials.[93] Similar techniques have been utilized to spatially map areas of differing bonding states in carbon-carbon multilayers.[94] Du Chesne[95] has also reviewed a number of applications of these techniques to polymer systems, and Varlot *et al.* have employed spectroscopic imaging to characterize the morphology of a tri-phase polymer blend.[96] Finally, Daniels *et al.* showed that subtle differences in the valence plasmon response at relatively low energy-loss (*i.e.* 5 eV to 50 eV) could be used to quantitatively map the local distribution of chemical phases and physical properties such as Young's modulus.[97]

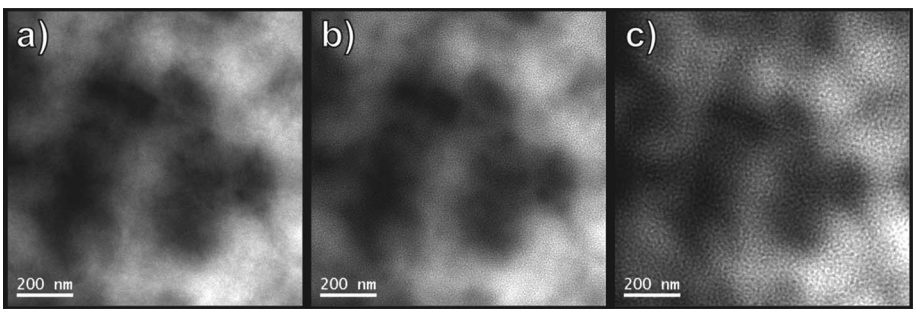

Fig. 7 Zero-loss filtered, bright-field TEM images of a P3HT:PCBM blend film acquired at varying objective lens defocus values: (a) 0 μm, (b) −5 μm, and (c) −25 μm.

Finally, the Midgley group has combined their previous demonstrations that EF-TEM was a viable basis for electron tomography[98,99] of solid state materials with the low-loss spectroscopy of Daniels *et al.*[97] to analyze an organic nanocomposite consisting of a single-walled carbon nanotube embededed in a matrix of nylon 6,6.[100] While BF-TEM was incapable of producing sufficient contrast from the two materials, low-loss EF-TEM tomography resulted in a quantitative, 3-D model of this composite.

In a recent paper,[101] we have detailed our effort to employ these techniques for the 3-D characterization of an OPV film based on P3HT:PCBM. These films were fabricated *via* a protocol similar to that described previously by Yang and co-workers.[102] A P3HT:PCBM BHJ film was prepared from 1,2-dichlorobenzene (DCB) solution. The solution was spin-coated onto PEDOT:PSS atop indium tin oxide (ITO) coated glass. A slow drying procedure was used to produce a BHJ that had previously been found to exhibit power conversion efficiencies of greater than.[29] A second BHJ film was produced by spin-coating an identical substrate from a solution of P3HT and PCBM in chlorobenzene (CB).

Fig. 8 depicts a series of images acquired from the DCB and CB films using various signals. In both cases, the BF-TEM images (Fig. 8a) reveal little morphological detail save that related to film thickness and roughness. In contrast, EF-TEM images acquired from either side of the bulk-plasmon region ($\approx$ 25 eV loss) were found to produce excellent contrast between the two materials. Hyperspectral imaging in conjunction with principal component analysis were used to unambiguously assign the spectral features to P3HT-rich and PCBM-rich regions, as well as to identify the optimum energy channels to collect for maximum contrast: a 5 eV wide slit centered at 19 eV for P3HT and at 29 eV for PCBM). The result of acquiring images using these parameters from both films is shown in Fig. 8b and Figure 8c, respectively. Finally, the maximum contrast images produced by taking the ratio of the 19 eV image to the 29 eV image are shown in (Fig. 8d). Clearly, the choice of solvent has a strong effect on the resulting morphology, as the DCB film contains a PCBM phase occupying the interstitial region defined by a fibrillar network of P3HT. In contrast, no elongated structures were found in the CB film. Instead, the P3HT-rich domains were nodular, surrounded by a matrix of PCBM-rich material. It is striking to note the radically different morphologies present in these two films, especially in light of the fact that both preparation routes have been reported to produce devices of comparable efficiencies.

At present, it is difficult to quantitatively describe the chemical makeup of the regions revealed by EF-TEM imaging, as the low-loss response of the material is complex and significant spectral overlap does exist. Since it is now well known that solid-solutions of P3HT in PCBM can exist up to a significant mass fraction,[34,52,68,70,71] it seems likely that varying degrees of intermixing could be present in one or both of these films. However, the ability to unambiguously reveal the microstructure of BHJ films make the EF-TEM approach invaluable to their characterization, especially as new materials come to be studied.

Finally, we have also previously shown the applicability of this signal to three-dimensional characterization *via* electron tomography. The results of such an analysis can be seen in Fig. 9, which depicts several slices extracted from various depths of an EF-TEM tomogram of the DCB film previously discussed. The in-plane distribution of the P3HT fibrils is clearly revealed throughout the thickness of the film, and largely matches that reported previously using BF-TEM based tomography. However, whereas significant vertical phase segregation was reported in the previous study of a similar film, no such vertical segregation was detected specimen using the present techniques.

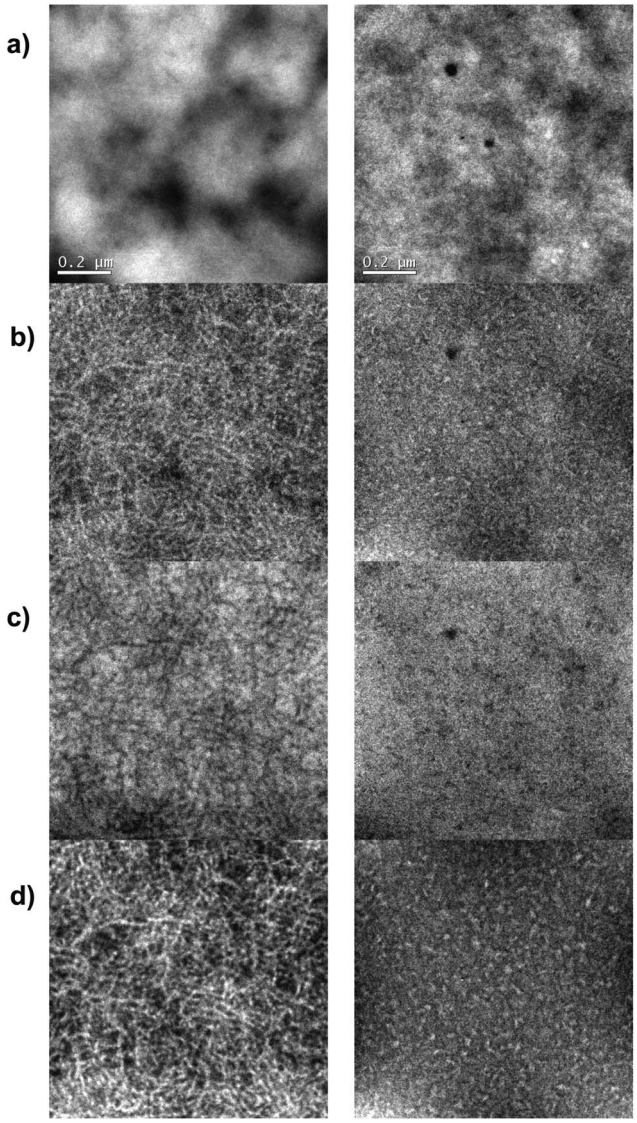

Fig. 8 Comparison of images acquired using various signals from P3HT:PCBM BHJ films spun from *ortho*-dichlorobenze (left) and chlorobenzene (right). (a) BF-TEM, (b) P3HT-sensitive EF-TEM (E = 19 eV, ΔE = 5 eV), and (c) PCBM-sensitive EF-TEM (E = 29 eV, ΔE = 5 eV). Also shown are the maximum contrast images (d), produced by taking the ratio of image (b) to image (c).

More recently, a similar low-loss EF-TEM approach to BHJ characterization has been utilized by Drummy *et al.*[103] By coupling this analysis with high-resolution lattice imaging under cryogenic conditions, the authors were able to elucidate the relationship between the mesoscale phase separation behavior and the underlying crystalline orientation within the fibrils themselves. Similarly, Pfannmoller *et al.* have utilized low-loss imaging in conjunction with a monochromated electron beam in

Fig. 9 Slices extracted at various vertical depths from a reconstructed EF-TEM tomogram of P3HT:PCBM BHJ film spun from DCB. The fibrillar structure present near the top (left), middle (center), and bottom (right) of the film is clearly revealed, and no vertical segregation was observed.

order to distinguish between three regions in the BHJ layer: the P3HT and PCBM phases first imaged in our work, but, importantly, a third, homogeneously mixed composite phase, as well.[104] Finally, Gomez and co-workers[105] have applied core-loss EF-TEM mapping of the sulfur and carbon content of P3HT:PCBM films to quantitatively describe the miscibility of the two materials and relate it to the morphological developments during heat treatment. This body of work shows the power of energy-filtered TEM imaging and EELS-based analysis in general for the morphological characterization of BHJ films, and should pave the way to a new understanding of the fundamental relationships between structure, processing, and device performance.

5. Summary and outlook

The importance of nanoscale structure in BHJ films has certainly been recognized, and a great deal of effort has been invested in measurements to correlate that nanoscale structure to the power conversion efficiency and lifetime of OPV devices. Robust correlations that can be reproduced across labs have, however, been elusive. Uneven implementation and interpretation of nanoscale structure measurements is partially responsible for this state of affairs. It must be recognized that differences in materials supply (purity, molecular mass, polydispersity, regioregularity) as well as processing variations due to uncontrolled or unreported variables also share some blame. With the proper selection, execution, and interpretation of measurements that address key aspects of nanoscale structure, even these variables can potentially be eliminated or modeled, and robust correlations should emerge. A potentially useful theme in structure measurement is the application of multiple techniques with simultaneous quantitative analysis. When combined with reasonable assumptions, this strategy can deliver quantitative structure metrics that cannot be extracted from the data of any of the techniques alone.[106] Another significant emerging measurement thrust is the effort to apply nanoscale structure measurements *during* film solidification. The ability to describe nanoscale structure evolution over time would lead to a far greater understanding of how to control it, which should greatly accelerate OPV technology development by informing research vectors ranging from chemical synthesis, to formulation, to module fabrication. The result should be a faster convergence of experimental device capabilities with the great theoretical promise that OPV technology has held since its inception.

References

1 C. J. Brabec, S. Gowrisanker, J. J. M. Halls, D. Laird, S. J. Jia and S. P. Williams, *Adv. Mater.*, 2010, **22**, 3839.
2 A. Facchetti, *Chem. Mater.*, 2011, **23**, 733.
3 J.-L. Bredas and J. R. Durrant, *Acc. Chem. Res.*, 2009, **42**, 1689.
4 G. Dennler, M. C. Scharber and C. J. Brabec, *Adv. Mater.*, 2009, **21**, 1323.
5 R. F. Service, *Science*, 2011, **332**, 293.
6 Y.-J. Cheng, S.-H. Yang and C.-S. Hsu, *Chem. Rev.*, 2009, **109**, 5868.
7 J. Chen and Y. Cao, *Acc. Chem. Res.*, 2009, **42**, 1709.
8 J. Peet, A. J. Heeger and G. C. Bazan, *Acc. Chem. Res.*, 2009, **42**, 1700.
9 Y. Zheng and J. G. Xue, *Polym. Rev.*, 2010, **50**, 420.
10 B. Walker, C. Kim and T. Q. Nguyen, *Chem. Mater.*, 2011, **23**, 470.
11 R. Steim, F. R. Kogler and C. J. Brabec, *J. Mater. Chem.*, 2010, **20**, 2499.
12 W. J. Potscavage, A. Sharma and B. Kippelen, *Acc. Chem. Res.*, 2009, **42**, 1758.
13 P. Heremans, D. Cheyns and B. P. Rand, *Acc. Chem. Res.*, 2009, **42**, 1740.
14 X. Yang and J. Loos, *Macromolecules*, 2007, **40**, 1353.
15 R. Giridharagopal and D. S. Ginger, *J. Phys. Chem. Lett.*, 2010, **1**, 1160.
16 A. Pivrikas, H. Neugebauer and N. S. Sariciftci, *Sol. Energy*, 2011, **85**, 1226.
17 M. A. Ruderer and P. Muller-Buschbaum, *Soft Matter*, 2011, **7**, 5482.
18 C. J. Brabec, M. Heeney, I. McCulloch and J. Nelson, *Chem. Soc. Rev.*, 2011, **40**, 1185.
19 A. J. Moule and K. Meerholz, *Adv. Funct. Mater.*, 2009, **19**, 3028.
20 M. T. Dang, L. Hirsch and G. Wantz, *Adv. Mater.*, 2011, **23**, 3597–3602.
21 Y. Kim, S. A. Choulis, J. Nelson and D. D. C. Bradley, *Appl. Phys. Lett.*, 2005, **86**, 063502.
22 E. L. Ratcliff, B. Zacher and N. R. Armstrong, *J. Phys. Chem. Lett.*, 2011, **2**, 1337.
23 L. M. Chen, Z. Xu, Z. R. Hong and Y. Yang, *J. Mater. Chem.*, 2010, **20**, 2575.
24 J. F. Watts and J. Wolstenholme, *An Introduction to Surface Analysis by XPS and AES*, 2nd edn, Wiley, 2003.
25 J. Stöhr. *NEXAFS Spectroscopy*, Vol. 392, Springer-Verlag, 1992.
26 D. M. DeLongchamp, R. J. Kline, D. A. Fischer, L. J. Richter and M. F. Toney, *Adv. Mater.*, 2011, **23**, 319.
27 A. Salleo, R. J. Kline, D. M. DeLongchamp and M. L. Chabinyc, *Adv. Mater.*, 2010, **22**, 3812.
28 Z. Xu, L.-M. Chen, G. Yang, C.-H. Huang, J. Hou, Y. Wu, G. Li, C.-S. Hsu and Y. Yang, *Adv. Funct. Mater.*, 2009, **19**, 1227–1234.
29 D. S. Germack, C. K. Chan, B. H. Hamadani, L. J. Richter, D. A. Fischer, D. J. Gundlach and D. M. DeLongchamp, *Appl. Phys. Lett.*, 2009, **94**, 233303.
30 M. P. Felicissimo, D. Jarzab, M. Gorgoi, M. Forster, U. Scherf, M. C. Scharber, S. Svensson, P. Rudolf and M. A. Loi, *J. Mater. Chem.*, 2009, **19**, 4899.
31 B. F. Xue, B. Vaughan, C. H. Poh, K. B. Burke, L. Thomsen, A. Stapleton, X. J. Zhou, G. W. Bryant, W. Belcher and P. C. Dastoor, *J. Phys. Chem. C*, 2010, **114**, 15797.

32 A. S. Anselmo, L. Lindgren, J. Rysz, A. Bernasik, A. Budkowski, M. R. Andersson, K. Svensson, J. van Stam and E. Moons, *Chem. Mater.*, 2011, **23**, 2295.
33 A. F. Tillack, K. M. Noone, B. A. MacLeod, D. Nordlund, K. P. Nagle, J. A. Bradley, S. K. Hau, H. L. Yip, A. K. Y. Jen, G. T. Seidler and D. S. Ginger, *ACS Appl. Mater. Interfaces*, 2011, **3**, 726.
34 D. Chen, F. Liu, C. Wang, A. Nakahara and T. P. Russell, *Nano Lett.*, 2011, **11**, 2071.
35 A. H. Rice, R. Giridharagopal, S. X. Zheng, F. S. Ohuchi, D. S. Ginger and C. K. Luscombe, *ACS Nano*, 2011, **5**, 3132.
36 D. S. Germack, C. K. Chan, R. J. Kline, D. A. Fischer, D. J. Gundlach, M. F. Toney, L. J. Richter and D. M. DeLongchamp, *Macromolecules*, 2010, **43**, 3828.
37 W. C. Tsoi, S. J. Spencer, L. Yang, A. M. Ballantyne, P. G. Nicholson, A. Turnbull, A. G. Shard, C. E. Murphy, D. D. C. Bradley, J. Nelson and J.-S. Kim, *Macromolecules*, 2011, **44**, 2944.
38 D. A. Chen, A. Nakahara, D. G. Wei, D. Nordlund and T. P. Russell, *Nano Lett.*, 2011, **11**, 561.
39 J. Daillant and A. Gibaud, in *Lect. Notes Phys* 362, Springer, 2009.
40 R. M. A. Azzam and N. M. Bashara, *Ellipsometry and Polarized Light* 558 North Holland, 1988.
41 J. W. Kiel, B. J. Kirby, C. F. Majkrzak, B. B. Maranville and M. E. Mackay, *Soft Matter*, 2010, **6**, 641.
42 J. W. Kiel, M. E. Mackay, B. J. Kirby, B. B. Maranville and C. F. Majkrzak, *J. Chem. Phys.*, 2010, **133**, 074902.
43 A. J. Parnell, A. D. F. Dunbar, A. J. Pearson, P. A. Staniec, A. J. C. Dennison, H. Hamamatsu, M. W. A. Skoda, D. G. Lidzey and R. A. L. Jones, *Adv. Mater.*, 2010, **22**, 2444.
44 C. Wang, A. Garcia, H. P. Yan, K. E. Sohn, A. Hexemer, T. Q. Nguyen, G. C. Bazan, E. J. Kramer and H. Ade, *J. Am. Chem. Soc.*, 2009, **131**, 12538.
45 H. P. Yan, S. Swaraj, C. Wang, I. Hwang, N. C. Greenham, C. Groves, H. Ade and C. R. McNeill, *Adv. Funct. Mater.*, 2010, **20**, 4329.
46 A. Ng, C. H. Li, M. K. Fung, A. B. Djurisic, J. A. Zapien, W. K. Chan, K. Y. Cheung and W. Y. Wong, *J. Phys. Chem. C*, 2010, **114**, 15094.
47 M. Campoy-Quiles, T. Ferenczi, T. Agostinelli, P. G. Etchegoin, T. D. Anthopolous, P. N. Stavrinou, D. D. C. Bradley and J. Nelson, *Nat. Mater.*, 2008, **7**, 158.
48 M. V. Madsen, K. O. Sylvester-Hvid, B. Dastmalchi, K. Hingerl, K. Norrman, T. Tromholt, M. Manceau, D. Angmo and F. C. Krebs, *J. Phys. Chem. C*, 2011, **115**, 10817.
49 G. Li, V. Shrotriya, J. S. Huang, Y. Yao, T. Moriarty, K. Emery and Y. Yang, *Nat. Mater.*, 2005, **4**, 864.
50 H. Hutter, in *Surface and Thin Film Analysis: A Compendium of Principles, Instrumentation, and Applications*, Vol. 2, eds G. Friedbacher & H. Bubert, ch. 9, Wiley-VCH Verlag GmbH & Co. KGaA, 2011.
51 J. N. Audinot, P. Leveque, R. Bechara, N. Leclerc, J. Guillot, H. N. Migeon, G. Hadziioannou and T. Heiser, *Surf. Interface Anal.*, 2010, **42**, 1010.
52 B. A. Collins, E. Gann, L. Guignard, X. He, C. R. McNeill and H. Ade, *J. Phys. Chem. Lett.*, 2010, **1**, 3160.
53 C. M. Bjorstrom, S. Nilsson, A. Bernasik, A. Budkowski, M. Andersson, K. O. Magnusson and E. Moons, *Appl. Surf. Sci.*, 2007, **253**, 3906.
54 A. Kumar, G. Li, Z. R. Hong and Y. Yang, *Nanotechnology*, 2009, **20**, 165202.
55 J. Y. Oh, W. S. Jang, T. I. Lee, J. M. Myoung and H. K. Baik, *Appl. Phys. Lett.*, 2011, **98**, 023303.
56 S. K. Hau, H. L. Yip and A. K. Y. Jen, *Polym. Rev.*, 2010, **50**, 474.
57 F. J. Zhang, X. W. Xu, W. H. Tang, J. Zhang, Z. L. Zhuo, J. Wang, Z. Xu and Y. S. Wang, *Sol. Energy Mater. Sol. Cells*, 2011, **95**, 1785.
58 H. Wang, E. D. Gomez, J. Kim, Z. L. Guan, C. Jaye, D. A. Fischer, A. Kahn and Y. L. Loo, *Chem. Mater.*, 2011, **23**, 2020.
59 A. Orimo, K. Masuda, S. Honda, H. Benten, S. Ito, H. Ohkita and H. Tsuji, *Appl. Phys. Lett.*, 2010, **96**, 043305.
60 C. He, D. S. Germack, R. J. Kline, D. M. Delongchamp, D. A. Fischer, C. R. Snyder, M. F. Toney, J. G. Kushmerick and L. J. Richter, *Sol. Energy Mater. Sol. Cells*, 2011, **95**, 1375.
61 L. Y. Park, A. M. Munro and D. S. Ginger, *J. Am. Chem. Soc.*, 2008, **130**, 15916.
62 D. C. Coffey, O. G. Reid, D. B. Rodovsky, G. P. Bartholomew and D. S. Ginger, *Nano Lett.*, 2007, **7**, 738.
63 B. H. Hamadani, S. Jung, P. M. Haney, L. J. Richter and N. B. Zhitenev, *Nano Lett.*, 2010, **10**, 1611.
64 W. C. Tsoi, P. G. Nicholson, J. S. Kim, D. Roy, T. L. Burnett, C. E. Murphy, J. Nelson, D. D. C. Bradley, J.-S. Kim and F. A. Castro, *Energy Environ. Sci.*, 2011, **4**, 3646.
65 C. Groves, O. G. Reid and D. S. Ginger, *Acc. Chem. Res.*, 2010, **43**, 612.
66 O. G. Reid, H. Xin, S. A. Jenekhe and D. S. Ginger, *J. Appl. Phys.*, 2010, **108**, 084320.
67 N. Blouin, A. Michaud and M. Leclerc, *Adv. Mater.*, 2007, **19**, 2295.
68 K. H. Lee, P. E. Schwenn, A. R. G. Smith, H. Cavaye, P. E. Shaw, M. James, K. B. Krueger, I. R. Gentle, P. Meredith and P. L. Burn, *Adv. Mater.*, 2011, **23**, 766.
69 D. Muhlbacher, M. Scharber, M. Morana, Z. G. Zhu, D. Waller, R. Gaudiana and C. Brabec, *Adv. Mater.*, 2006, **18**, 2884.
70 N. D. Treat, M. A. Brady, G. Smith, M. F. Toney, E. J. Kramer, C. J. Hawker and M. L. Chabinyc, *Adv. Energy Mater.*, 2011, **1**, 82.
71 B. Watts, W. J. Belcher, L. Thomsen, H. Ade and P. C. Dastoor, *Macromolecules*, 2009, **42**, 8392.
72 J. S. Moon, C. J. Takacs, Y. M. Sun and A. J. Heeger, *Nano Lett.*, 2011, **11**, 1036.
73 J. Clark, J. F. Chang, F. C. Spano, R. H. Friend and C. Silva, *Appl. Phys. Lett.*, 2009, **94**, 163306.
74 W. C. Tsoi, D. T. James, J. S. Kim, P. G. Nicholson, C. E. Murphy, D. D. C. Bradley, J. Nelson and J.-S. Kim, *J. Am. Chem. Soc.*, 2011, **133**, 9834.
75 R. C. Nieuwendaal, C. R. Snyder, R. J. Kline, E. K. Lin, D. L. VanderHart and D. M. DeLongchamp, *Chem. Mater.*, 2010, **22**, 2930–2936.
76 R. A. Street, J. E. Northrup and A. Salleo, *Phys. Rev. B: Condens. Matter Mater. Phys.*, 2005, **71**, 165202.
77 N. Tessler, Y. Preezant, N. Rappaport and Y. Roichman, *Adv. Mater.*, 2009, **21**, 2741.
78 H. Sirringhaus, M. Bird, T. Richards and N. Zhao, *Adv. Mater.*, 2010, **22**, 3893.
79 M. C. Gurau, D. M. Delongchamp, B. M. Vogel, E. K. Lin, D. A. Fischer, S. Sambasivan and L. J. Richter, *Langmuir*, 2007, **23**, 834.
80 D. M. DeLongchamp, R. J. Kline, E. K. Lin, D. A. Fischer, L. J. Richter, L. A. Lucas, M. Heeney, I. McCulloch and J. E. Northrup, *Adv. Mater.*, 2007, **19**, 833.
81 B. D. Cullity and S. R. Stock, *Elements of X-Ray Diffraction*, 3rd edn, Prentice Hall, 2001.
82 J. L. Baker, L. H. Jimison, S. Mannsfeld, S. Volkman, S. Yin, V. Subramanian, A. Salleo, A. P. Alivisatos and M. F. Toney, *Langmuir*, 2010, **26**, 9146.
83 L. H. Jimison, *Understanding microstructure and charge transport in semi crystalline polythiophenes*, Ph. D. thesis, Stanford University, 2011.
84 E. D. Gomez, K. P. Barteau, H. Wang, M. F. Toney and Y. L. Loo, *Chem. Commun.*, 2011, **47**, 436.
85 J. Rivnay, R. Steyrleuthner, L. H. Jimison, A. Casadei, Z. H. Chen, M. F. Toney, A. Facchetti, D. Neher and A. Salleo, *Macromolecules*, 2011, **44**, 5246.
86 E. Verploegen, R. Mondal, C. J. Bettinger, S. Sok, M. F. Toney and Z. A. Bao, *Adv. Funct. Mater.*, 2010, **20**, 3519.
87 S. Lilliu, T. Agostinelli, E. Pires, M. Hampton, J. Nelson and J. E. Macdonald, *Macromolecules*, 2011, **44**, 2725.
88 P. Peumans, S. Uchida and S. R. Forrest, *Nature*, 2003, **425**, 158.
89 S. S. van Bavel, E. Sourty, G. de With and J. Loos, *Nano Lett.*, 2009, **9**, 507.
90 S. van Bavel, E. Sourty, G. de With, S. Veenstra and J. Loos, *J. Mater. Chem.*, 2009, **19**, 5388.
91 S. Miller, G. Fanchini, Y. Y. Lin, C. Li, C. W. Chen, W. F. Su and M. Chhowalla, *J. Mater. Chem.*, 2008, **18**, 306.
92 S. Yakovlev and M. Libera, *Micron*, 2008, **39**, 734.
93 K. Siangchaew and M. Libera, *Microsc. Microanal.*, 1997, **3**, 530.
94 M. Bosman, V. J. Keast, M. Watanabe, D. G. McCulloch, M. Shakerzadeh, E. H. T. Teo and B. K. Tay, *Carbon*, 2009, **47**, 94.
95 A. Du Chesne, *Macromol. Chem. Phys.*, 1999, **200**, 1813.
96 K. Varlot, J. M. Martin and C. Quet, *Polymer*, 2000, **41**, 4599.
97 H. R. Daniels, R. Brydson, A. Brown and B. Rand, *Ultramicroscopy*, 2003, **96**, 547.

98 P. A. Midgley and M. Weyland, *Ultramicroscopy*, 2003, **96**, 413.
99 M. Weyland and P. A. Midgley, *Microsc. Microanal.*, 2003, **9**, 542.
100 M. H. Gass, K. K. K. Koziol, A. H. Windle and P. A. Midgley, *Nano Lett.*, 2006, **6**, 376.
101 A. A. Herzing, L. J. Richter and I. M. Anderson, *J. Phys. Chem. C*, 2010, **114**, 17501.
102 G. Li, Y. Yao, H. Yang, V. Shrotriya, G. Yang and Y. Yang, *Adv. Funct. Mater.*, 2007, **17**, 1636.
103 L. F. Drummy, R. J. Davis, D. L. Moore, M. Durstock, R. A. Vaia and J. W. P. Hsu, *Chem. Mater.*, 2011, **23**, 907.
104 M. Pfannmöller, H. Flügge, G. Benner, I. Wacker, C. Sommer, M. Hanselmann, S. Schmale, H. Schmidt, F. a. Hamprecht, T. Rabe, W. Kowalsky and R. R. Schröder, *Nano Lett.*, 2011, **11**, 3099–3107.
105 D. R. Kozub, K. Vakhshouri, L. M. Orme, C. Wang, A. Hexemer and E. D. Gomez, *Macromolecules*, 2011, **44**, 5722.
106 M. R. Hammond, R. J. Kline, A. A. Herzing, L. J. Richter, D. S. Germack, H. W. Ro, C. L. Soles, D. A. Fischer, T. Xu, L. P. Yu, M. F. Toney and D. M. DeLongchamp, *ACS Nano*, 2011, **5**, 8248.